

Article

Simultaneously Enhanced Strength, Toughness and Ductility of Cast 40Cr Steels Strengthened by Trace Biphase $\text{TiC}_x\text{-TiB}_2$ Nanoparticles

Chuan-Lu Li ^{1,2}, Feng Qiu ^{1,2,3,*} , Fang Chang ^{1,2}, Xu-Min Zhao ^{1,2}, Run Geng ^{1,2}, Hong-Yu Yang ⁴, Qing-Long Zhao ^{1,2}  and Qi-Chuan Jiang ^{1,2,*}

¹ State Key Laboratory of Automotive Simulation and Control, Jilin University, Renmin Street NO. 5988, Changchun 130025, China; chuanluli@126.com (C.-L.L.); changfang@jlu.edu.cn (F.C.); zhaoxm15@163.com (X.-M.Z.); gengrun@126.com (R.G.); zhaoqinglong@jlu.edu.cn (Q.-L.Z.)

² Key Laboratory of Automobile Materials, Ministry of Education and Department of Materials Science and Engineering, Jilin University, Renmin Street NO. 5988, Changchun 130025, China

³ Qingdao Automotive Research Institute of Jilin University, Renmin Street NO. 5988, Changchun 130025, China

⁴ School of Materials Science and Engineering, Jiangsu University of Science and Technology, Zhenjiang 212003, China; yanghy@just.edu.cn

* Correspondence: qiufeng@jlu.edu.cn (F.Q.); Jiangqc@jlu.edu.cn (Q.-C.J.);
Tel.: +86-431-8509-5592 (F.Q.); +86-431-8509-4699 (Q.-C.J.)

Received: 10 August 2018; Accepted: 4 September 2018; Published: 9 September 2018



Abstract: Simultaneously improving the strength, toughness, and ductility of cast steels has always been a difficult problem for researchers. Biphase $\text{TiC}_x\text{-TiB}_2$ nanoparticle-reinforced cast steels are prepared by adding in situ nanosized biphase $\text{TiC}_x\text{-TiB}_2/\text{Al}$ master alloy during the casting process. The experimental results show that a series of significant changes take place in the microstructure of the steel: the ferrite-pearlite structure of the as-cast steels and the bainite structure of the steels after heat treatment are refined, the grain size is reduced, and the content of nanoparticles is increased. Promotion of nucleation and inhibition of dendrite growth by biphase $\text{TiC}_x\text{-TiB}_2$ nanoparticles leads to a refinement of the microstructure. The fine microstructure with evenly dispersed nanoparticles offers better properties [yield strength (1246 MPa), tensile strength (1469 MPa), fracture strain (9.4%), impact toughness (20.3 J/cm²) and hardness (41 HRC)] for the steel with 0.018 wt.% biphase $\text{TiC}_x\text{-TiB}_2$ nanoparticles, which are increased by 15.4%, 31.2%, 4.4%, 11.5%, and 7.9% compared with the 40Cr steels. The higher content of nanoparticles provides higher strengths and hardness of the steel but are detrimental to ductility. The improved properties may be attributed to fine grain strengthening and the pinning effect of nanosized carbide on dislocations and grain boundaries. Through this work, it is known that the method of adding trace (0.018 wt.%) biphase $\text{TiC}_x\text{-TiB}_2$ nanoparticles during casting process can simultaneously improve the strength, toughness, as well as ductility of the cast steel.

Keywords: $\text{TiC}_x\text{-TiB}_2$ nanoparticles; grain refinement; mechanical property; strengthening mechanism

1. Introduction

Solving the problem of simultaneously improving the strength and toughness of cast steels is a long-term goal for researchers. In recent years, ceramic particles, such as TiC [1,2], TiB_2 [3,4], (NbTi)C [5] and other ceramics [6,7], have been used to enhance metallic materials because of their good thermal stability, high modulus, and good wettability with the metal matrix [6,8–11]. The outstanding role of ceramic particles in enhancing metal properties has aroused researchers' interest [12–15].

Sung-Mo Hong et al. found that nanosized TiC particles can refine the structure and increase the strength of SA-106B carbon steel [16]. S.W. Hu et al. found that TiC particles 2 μm in size can strengthen the hardness and wear resistance of manganese steel [17]. TiB₂ and TiC-reinforced steel matrix composites were produced through powder metallurgy, improving the wear properties of the composites [18–20]. Improved steel properties were expected to be obtained through the combination of TiB₂ and TiC particles. Spark plasma sintering was used to produce TiB₂-TiC-reinforced steel matrix composites [21]. Among the various methods, traditional casting is economical and convenient, with its high production efficiency and flexible product shape [22,23]. However, due to the large difference in specific gravity, agglomeration of nanoparticles and surface pollution of nanoparticles, it seems that the traditional casting method is not suitable for producing nanoceramic-reinforced steel. Because of these constraints, there have been few studies on enhancing the strength and toughness of cast steel with dual-phase nanosized ceramic particles (TiC_x-TiB₂). Therefore, it is meaningful to prepare TiC_x-TiB₂ nanoparticle-reinforced steel through traditional casting method.

In this work, we have innovatively added the in situ nanosized biphasic TiC_x-TiB₂/Al master alloy into the casting process to make trace (TiC_x-TiB₂) nanoparticle-reinforced cast steel. The master alloy, in which nanosized ceramic particles are uniformly dispersed, is prepared by the SHS (self-propagating high temperature synthesis) method. This work helps to solve the problem of floating, agglomerating, and surface contamination of ceramic particles in the steel and makes full use of the benefits of the dual-phase ceramic particles (TiC_x-TiB₂) and conventional casting methods. The experimental results show that the strength and toughness of the dual-phase ceramic particles-reinforced cast steel are simultaneously improved. The influence mechanisms of the ceramic particles on both microstructural evolution and properties improvement of steels have been fully analyzed and discussed. In this paper, the preparation methods show a large potential application value, and the analysis and discussion provide a valuable reference for subsequent researchers.

2. Materials and Methods

The main chemical composition of investigated 40Cr steel is displayed in Table 1. The nanosized TiC_x-TiB₂/Al master alloy was prepared through self-propagating high-temperature synthesis. First, Al (~13 μm), Ti (~25 μm), and B₄C (~1.5 μm) powders at a ratio corresponding to that of stoichiometric TiC and TiB₂ were sufficiently mixed in a ball mill at a speed of 50 rpm for 18 h. Second, the sufficiently mixed powders were cold pressed into cylindrical compacts ($\Phi = 28 \text{ mm}$; $h = 30 \text{ mm}$). Finally, a self-made vacuum thermal explosion furnace was used to initiate the self-propagating high-temperature synthesis (SHS) reaction in the compacts at a heating speed of about 30 K/min. and then at 900 °C for 10 min. After the reaction was completed, the nanosized TiC_x-TiB₂/Al master alloy was successfully produced. The molten steel melted in 5 kg-capacity medium frequency furnace (GW-0.3t, NHHY, Foshan, China) was poured into a ladle, in which the master alloy had been placed. The molten steel with the ceramic particles dispersed throughout was cast into the sand mold and then cooled to room temperature. The steels were kept at 950 °C for 90 min and oil quenched. Afterwards, the steels were kept at 200 °C for 480 min and air cooled to room temperature, as shown in Figure 1.

Table 1. Chemical composition of the 40Cr steel.

Element	C	Si	Mn	Cr	S	P	Fe
wt.%	0.41	0.25	0.65	0.95	0.004	0.018	Bal.

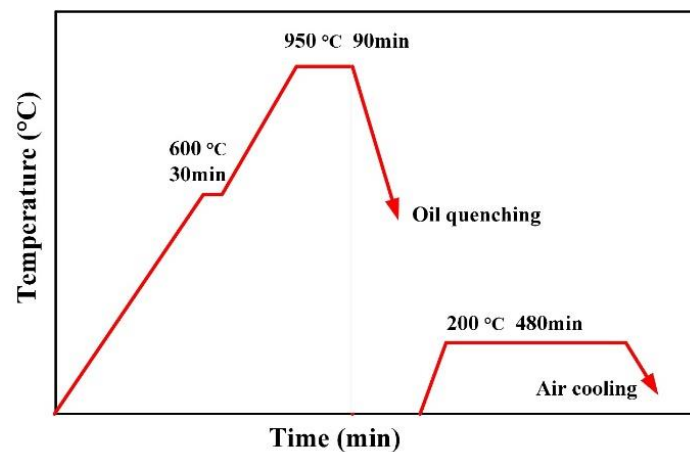


Figure 1. Heat treatment process diagram for cast steels.

The chemical composition of the investigated alloy was determined by direct-reading spectrometer (CX-9000, GLMY, WuXi, China). The ceramic particles extracted from the master alloy were characterized by X-ray diffraction (XRD, D/Max 2500PC Rigaku, Japan) and by field emission scanning electron microscopy (FESEM, JSM-6700F, JEOL, Tokyo, Japan). Samples after heat treatment were cut into dog-bone shaped tensile specimens (the specimens had a gauge length of 8 mm and cross-sectional area of 2.5 mm × 2 mm) and Charpy impact specimens (10 × 10 × 55 mm, U-notch). The samples used for optical microscopy (OM, Olympus PMG3, Tokyo, Japan) were polished and etched with a 5% nitric acid and 95% alcohol mixture. The samples designated for electron backscatter diffraction (EBSD, Oxford NordlysMax EBSD, Oxford, UK) analysis were electropolished in a mixture of 20% perchloric acid (Beijing Chemical Works, Beijing, China) and 80% acetic acid (Beijing Chemical Works, Beijing, China) at 30 V for 15 s. 0.3 μm was chosen as step size of EBSD scans. The TEM microstructure was acquired by using a JEOL microscope (JEM 2100F, JEOL, Tokyo, Japan). The tensile tests were performed on a servo hydraulic materials testing system (MTS 810, MTS Systems Corporation, Minneapolis, MN, USA). The standard Charpy impact test was conducted using a semiautomatic impact tester (JBW-300B, JNKH, Jinan, China). The fracture surfaces of the tensile and impact specimens were observed by means of scanning electron microscopy (SEM, VEGA 3 XMU, TESCAN, Brno, Czech Republic).

3. Results and Discussion

Figure 2a presents the XRD pattern of the nanosized biphased $\text{TiC}_x\text{-TiB}_2/\text{Al}$ master alloy, which shows that the master alloy mainly contains $\alpha\text{-Al}$, TiC , TiB_2 and a small amount of Al_3Ti . It can be determined that the SHS reaction is relatively complete, with only a small amount of Al_3Ti remaining. Figure 2b is a FESEM image of the mixed particles of TiC and TiB_2 obtained by extracting the nanosized $\text{TiC}_x\text{-TiB}_2/\text{Al}$ master alloy with hydrochloric acid. It can be seen that in addition to the spherical TiC particles, there are also hexagonal prisms or lamellar TiB_2 particles. The size statistics of the TiC_x and TiB_2 mixed particles in Figure 2b shows that the average grain size of the mixed particles is 190 nm. The nanoparticles are separated by aluminum, with no significant agglomeration with one another (Figure 2c,d). Then, the nanosized $\text{TiC}_x\text{-TiB}_2/\text{Al}$ master alloy was melted and gradually dispersed in the molten steel. The aluminum in the master alloy can also be simultaneously used as an oxygen scavenger to react with oxygen at a high temperature to form Al_2O_3 . Then, the Al_2O_3 is removed during the smelting process. This method not only successfully introduces nanoparticles into the molten steel but also contributes to the uniform dispersion of nanoparticles and to the removal of oxygen from the steel.

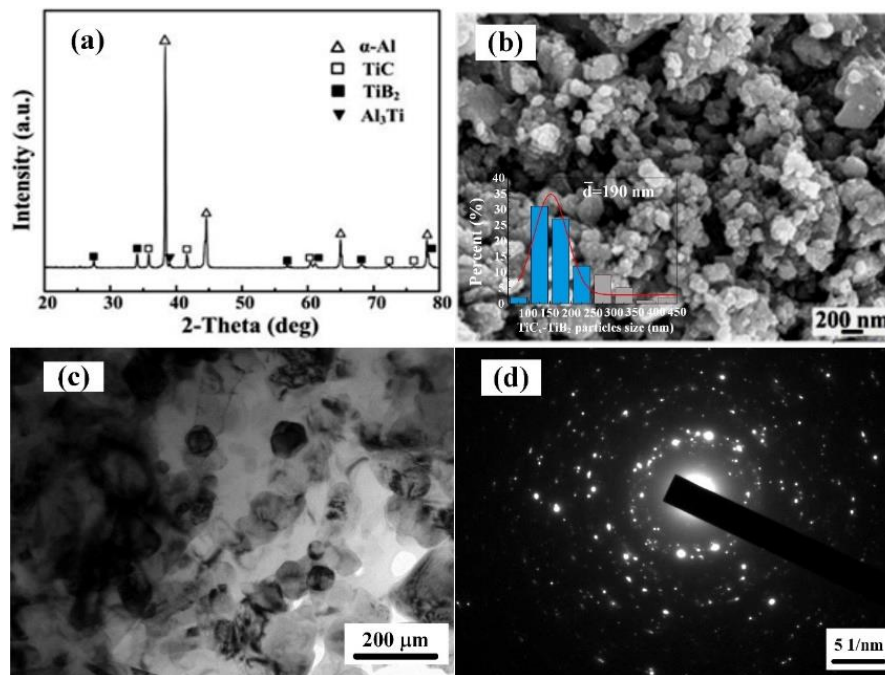


Figure 2. (a) XRD pattern of nano-sized TiC_x-TiB₂/Al master alloy, (b) morphologies and sizes analysis of the nano-sized TiC_x-TiB₂ particles in the nano-sized TiC_x-TiB₂/Al master alloy. TEM images (c) and electron diffraction patterns (d) of the nano-sized TiC_x-TiB₂/Al master alloy.

The typical ferrite-pearlite hybrid structure of the medium-carbon steel can be seen in Figure 3a. The bright area is pro-eutectoid ferrite, and the dark area is pearlite [24–26]. Because the carbon content of the steel is less than 0.77 wt.%, ferrite will be precipitated along the austenite grain boundary before the pearlite transformation. Therefore, the long strip ferrite is distributed on the boundary of the coarser pearlite group. After adding the 0.018 wt.% nanoceramic particles, it can clearly be seen that instead of the strip-shaped pro-eutectoid ferrite, the small pieces of ferrite dispersed inside the pearlite group increase, and the size of the pearlite group is also reduced (Figure 3b). When the content of nanoparticles in the steel is increased to 0.054 wt.%, smaller ferrite in the structure is distributed uniformly, and the pearlite structure is further refined (Figure 3c). It is known from the structure observed under the optical micrographs that the microstructure of the steel after heat treatment mainly contains lower bainite and a small amount of residual ferrite. The unevenly distributed particles with a large number of large white blocks can be seen in Figure 3d. In contrast, the lath ferrite and carbide in the microstructure of the steel, to which the 0.018 wt.% nanoparticles are added, are significantly finer and more uniform. More lath ferrites and carbides were observed in Figure 3f, but the lath ferrite is thicker than that in Figure 3e.

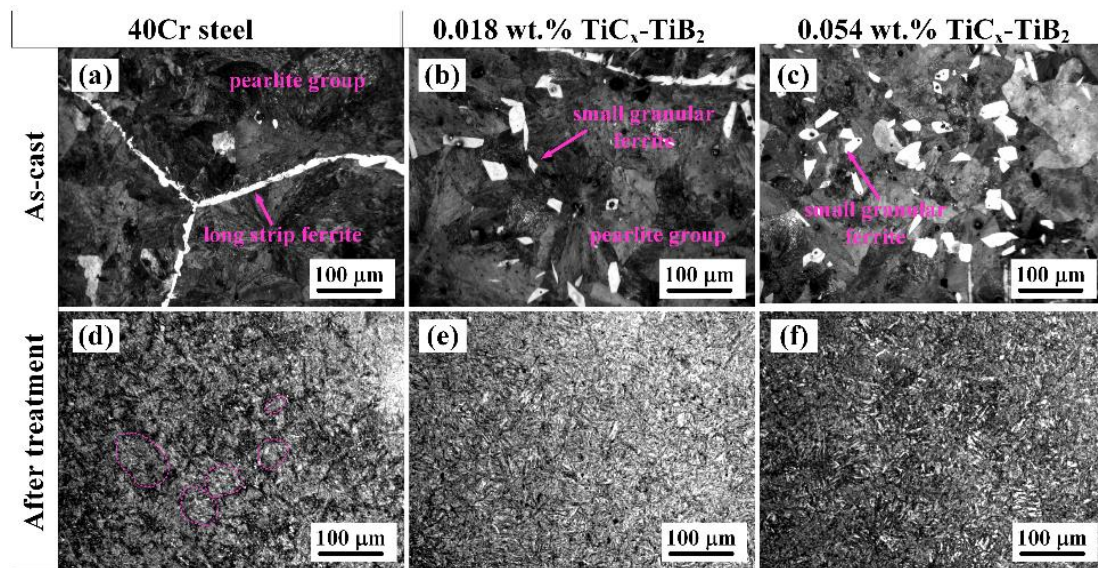


Figure 3. OM images of the as-cast steels (a–c), and steels after heat treatment (d–f).

The EBSD method was used to clarify the quantitative degree of grain refinement, as shown in Figure 4. The average grain size is refined from 9.12 μm in the 40Cr steel to 3.59 μm in the steel with 0.018 wt.% $\text{TiC}_x\text{-TiB}_2$ nanoparticles. The grain size of the steels with trace nanosized $\text{TiC}_x\text{-TiB}_2$ particles was refined by 60.6%. More importantly, the nanoparticles not only changed the cast microstructure of the steel but also refined the grain size of the steel after heat treatment.

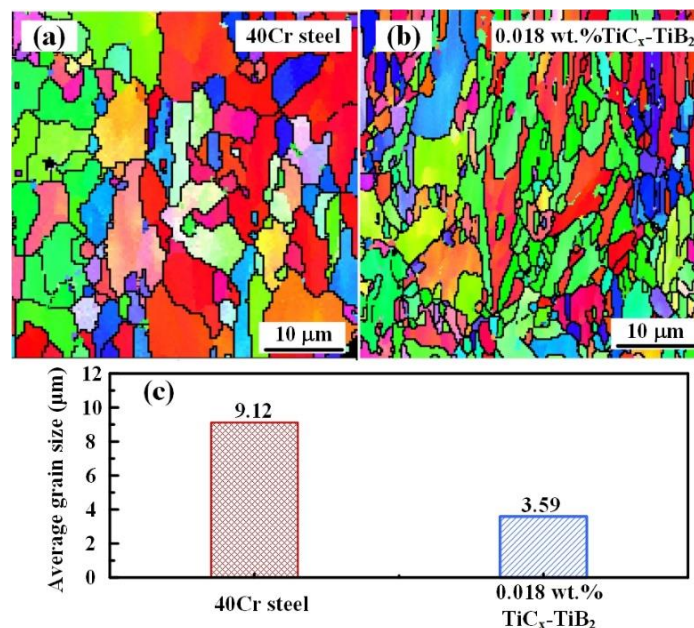


Figure 4. EBSD images of steels with $\text{TiC}_x\text{-TiB}_2$ particles contents of 0 wt.% (a) and 0.018 wt.% (b) after heat treatment. (c) shows the average grain size of (a,b).

The TEM images in Figure 5 show the differences in microstructures between the steels without nanosized $\text{TiC}_x\text{-TiB}_2$ particles and the 0.018 wt.% $\text{TiC}_x\text{-TiB}_2$ nanoparticle-reinforced steel. It is determined that a large number of carbide particles, of which the size is less than 100 nm, are evenly distributed in the microstructure of the 0.018 wt.% $\text{TiC}_x\text{-TiB}_2$ nanoparticle-reinforced steel in Figure 5b. On the contrary, a smaller amount of carbide particles is found in the microstructure of the steels without nanosized $\text{TiC}_x\text{-TiB}_2$ particles (Figure 5a).

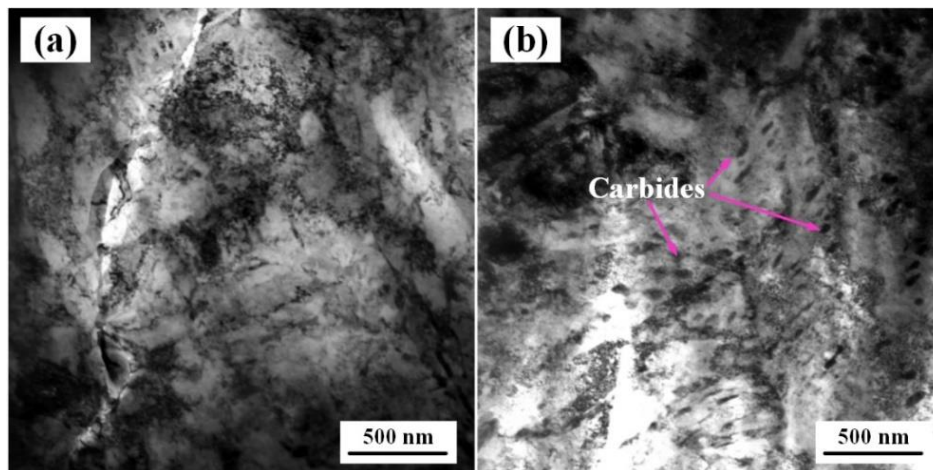


Figure 5. TEM images of steels without nano-sized $\text{TiC}_x\text{-TiB}_2$ particles (a) and steels with 0.018 wt.% $\text{TiC}_x\text{-TiB}_2$ nanoparticles (b).

TiC_x and TiB_2 have been proven to be effective austenitic heterogeneous nucleation sites [2,10,12]. Nanoparticles are successfully introduced and dispersed into the liquid steel herein. As shown in Figure 6, because structural undulations and energy fluctuations of the heterogeneous nucleation are small, nucleation occurs preferentially on the nanoparticles. Usually, larger-sized nanoparticles act as the nucleation site, while smaller-sized nanoparticles adsorb onto the solid-liquid interface and hinder the transition of the interface, thus inhibiting the growth of the dendrite [27]. The primary dendrites gradually grow, and finally, the material becomes completely austenitized. The size of the prior austenite grains seriously affects the later ferrite-pearlite structure and the bainite structure [28]. The increased grain boundaries due to austenite grain refinement and dispersed nanoparticles provide more precipitation sites for pro-eutectoid ferrite, which avoid the formation of long ferrite and limit the growth of pearlite. The most important process when the bainite transformation occurs is the diffusion of carbon. The rapid diffusion channels and thermal mismatches produced by the grain boundaries and nanoparticles promote the diffusion of carbon and the nucleation of carbides, so there are a large number of dispersed carbides throughout the structure.

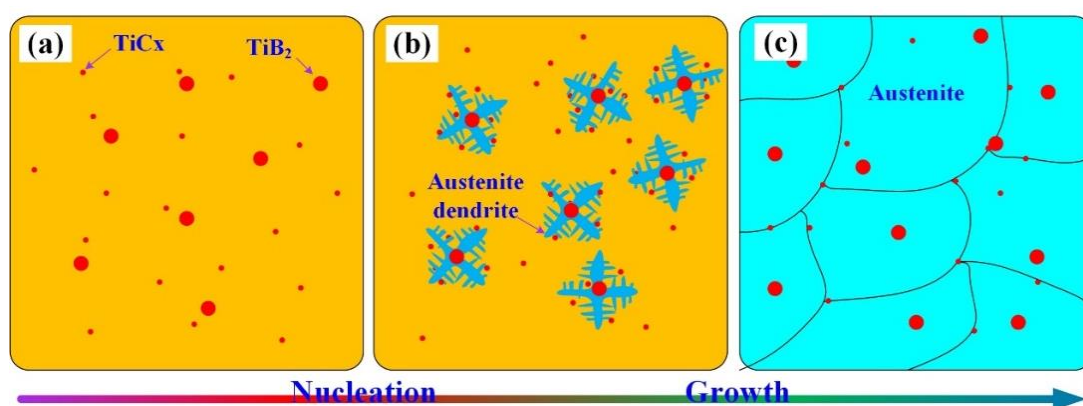


Figure 6. The effect of $\text{TiC}_x\text{-TiB}_2$ nanoparticles on the refinement of austenite. (a) Nanoparticles in molten steel; (b) Nucleation and growth of austenite; (c) Nanoparticles in austenite.

Figure 7 shows the tensile engineering stress-strain curves and fracture surfaces of the 40Cr steels with different $\text{TiC}_x\text{-TiB}_2$ nanoparticle contents. It is not difficult to determine from Figure 7a that the yield strength and tensile strength of the steel with nanoparticles are greatly improved. In addition to a large increase in the yield strength and tensile strength compared to the 40Cr steel, the fracture strain of the steel containing 0.018 wt.% $\text{TiC}_x\text{-TiB}_2$ nanoparticles is also improved. The yield and

tensile strengths of the steel with 0.054 wt.% nanoparticles added are further enhanced, but the fracture strain is obviously decreased. From Table 2 one can observe that the yield strength, tensile strength, and fracture strain of the 40Cr steel are 1080 MPa, 1120 MPa and 9%, respectively. Compared with the 40Cr steel, the yield strength (1246 MPa), tensile strength (1469 MPa), and fracture strain (9.4%) of the steel containing 0.018 wt.% $\text{TiC}_x\text{-TiB}_2$ nanoparticles are increased by 15.4%, 31.2% and 4.4%, respectively. The yield strength (1415 MPa) and tensile strength (1554 MPa) of the steel with 0.054 wt.% $\text{TiC}_x\text{-TiB}_2$ nanoparticles are increased by 31% and 38.8% compared with the 40Cr steel, respectively. The fracture surfaces (Figure 7b–d) also reflect the tensile properties of the material to some extent. There are some dimples with uneven sizes on the tensile fracture of the 40Cr steel, which shows a ductile fracture. The dimples on the fracture surface of the steel with 0.018 wt.% nanoparticles are more obvious, and the size is more uniform, but it is also a ductile fracture. However, there are fewer dimples on the fracture surface of the steel with 0.054 wt.% nanoparticles, and most of the areas have a rock or sugar-like morphology, which shows a brittle intergranular fracture. Owing to the increase of carbides inside and the refinement of grain size, hardness of steels with nanoparticles has increased, as Table 2 lists.

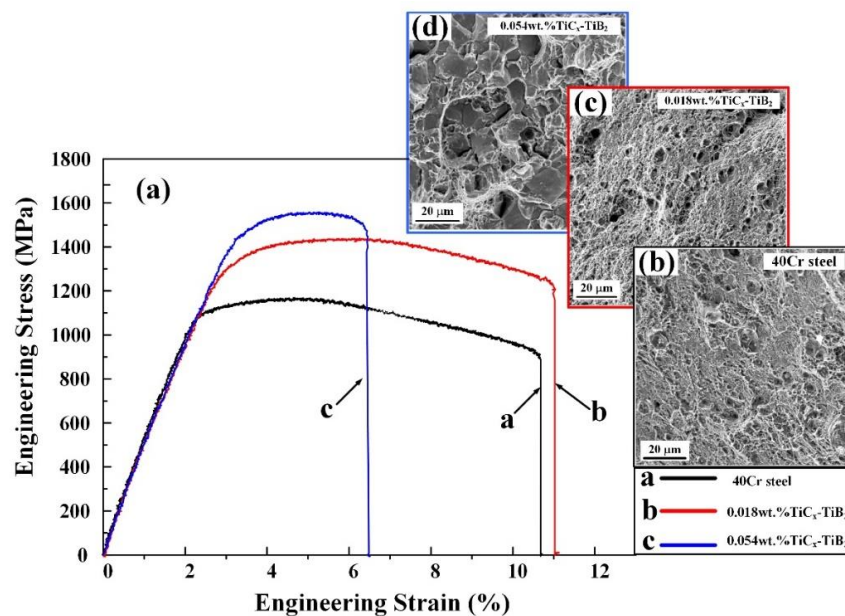


Figure 7. The tensile engineering stress-strain curves of steels with different $\text{TiC}_x\text{-TiB}_2$ nanoparticles content in (a), and the corresponding fracture surfaces in (b–d).

Table 2. Tensile properties, impact toughness and hardness of the steels with different content of $\text{TiC}_x\text{-TiB}_2$ nanoparticles.

Samples	$\sigma_{0.2}$ (MPa)	σ_{UTS} (MPa)	Fracture Strain ϵ_f (%)	ak (J/cm ²)	Hardness HRC
40Cr steels	1080 ⁺¹⁰ ₋₇₀	1120 ⁺²⁰ ₋₁₀	9.0 ^{+1.6} _{-2.0}	18.2 ± 0.85	38 ^{+1.5} _{-1.0}
0.018 wt.% $\text{TiC}_x + \text{TiB}_2$	1246 ⁺⁸ ₋₆	1469 ⁺²⁰ ₋₁₀	9.4 ^{+1.7} _{-1.0}	20.3 ± 1.66	41 ^{+1.1} _{-0.8}
0.054 wt.% $\text{TiC}_x + \text{TiB}_2$	1415 ⁺⁵ ₋₂	1554 ⁺⁸ ₋₃₅	5.56 ^{+0.8} _{-1.3}	13.8 ± 0.80	47 ^{+2.2} _{-2.1}

Figure 8 reflects the work-hardening ability of the steels with different $\text{TiC}_x\text{-TiB}_2$ nanoparticles contents. Combined with the analysis of Figure 7, it is determined that the yield strength of the 40Cr steel is low, the yielding occurs very quickly, and the work-hardening rate rapidly decreases after yielding. Compared with the 40Cr steel, the steel with 0.018 wt.% $\text{TiC}_x\text{-TiB}_2$ nanoparticles has a higher yield strength, and a higher work-hardening rate with the same plastic deformation after yielding. The steel with 0.054 wt.% $\text{TiC}_x\text{-TiB}_2$ nanoparticles has the highest yield strength, and the highest

work-hardening rate, but its work-hardening rate is less than the steel with 0.018 wt.% nanoparticles when the true strain at a value exceeding 4.5% as shown in Figure 8, and there is no buffering stage of the work-hardening rate similar to that of the steel with 0.018 wt.% $\text{TiC}_x\text{-TiB}_2$ nanoparticles.

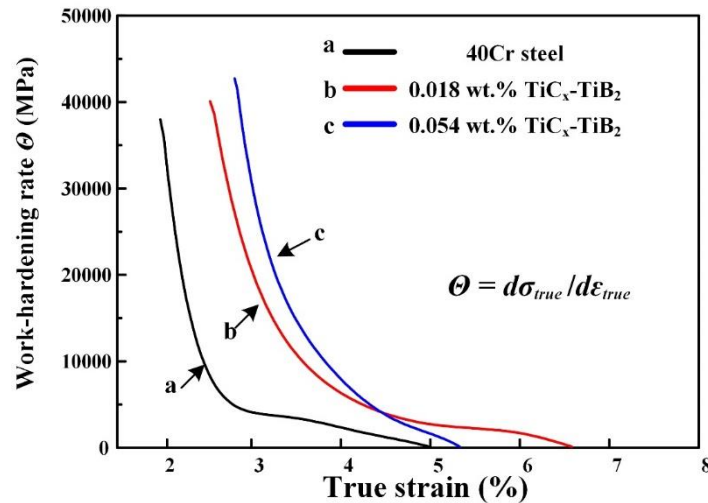


Figure 8. The corresponding work-hardening rate-true strain curves that were obtained from the tensile curve.

Figure 9 shows the impact properties and impact fracture morphologies of the steels with different contents of $\text{TiC}_x\text{-TiB}_2$ nanoparticles at room temperature. The impact toughness of steel with 0.018 wt.% $\text{TiC}_x\text{-TiB}_2$ nanoparticles is 11.5% higher than that of the 40Cr steel, but the impact toughness of the steel with 0.054 wt.% nanoparticles is reduced. Some of the reasons for this can be seen from the impact fracture surfaces in Figure 9. In the impact fracture surfaces of the 40Cr steel, the quasi-cleavage transgranular fracture is dominant, and there is a small intergranular fracture section. Except for a small amount of cleavage fracture, there are many dimples on the impact fracture of the steel with 0.018 wt.% $\text{TiC}_x\text{-TiB}_2$ nanoparticles, indicating that the impact toughness is better than that of the 40Cr steel. The fracture of the steel with 0.054 wt.% $\text{TiC}_x\text{-TiB}_2$ nanoparticles is dominated by brittle intergranular fracture and some cracks, which are unfavorable for the toughness of the material.

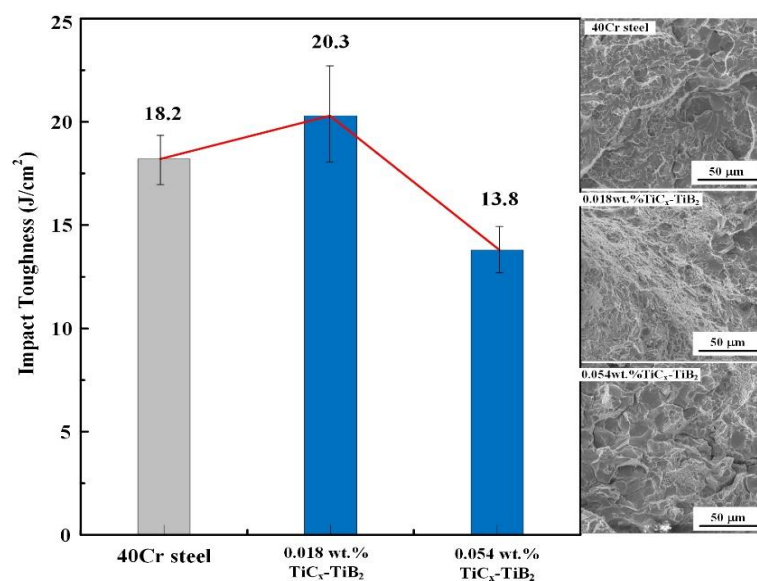


Figure 9. Impact toughness of steels with different contents of $\text{TiC}_x\text{-TiB}_2$ nanoparticles and the corresponding impact fracture surfaces.

According to the Hall-Petch formula, a smaller average grain size can result in a larger yield strength [29]. The difference in grain orientation on both sides of the grain boundary increases the slip resistance of the dislocation near the grain boundary and causes dislocations to accumulate at the grain boundary. According to the Orowan mechanism, a large number of dispersed carbides can hinder the movement of dislocations and cause an entanglement of the dislocations [30–33]. The dislocation loop will be left behind when dislocations pass through the carbides and nanoparticles, which produces a reaction force to the dislocation source. All of the above factors can improve the tensile strength of the steels. In a certain volume, the smaller grains size means a greater number of grains. The deformation is more uniform because it can be dispersed in more grains with the same amount of plastic deformation. On the other hand, when there is stress concentration in the material, voids tend to form in the weaker part. With the strain increasing, voids grow up, and adjacent voids gather together to form dimples. However, materials with uniform internal structure such as steels with 0.018 wt.% nanoparticles have more uniform distribution of vacancies when strain occurs, so the dimples on the fracture surface are more uniform and the size of dimples is larger before fracture. On the contrary, materials with less uniform internal structure, such as the matrix, tend to concentrate a large number of voids to form crack sources when strain occurs. Therefore, the ductility of steels with 0.018 wt.% nanoparticles is better than that of the matrix. Materials can withstand a large amount of deformation before breaking when fewer cracks caused by a stress concentration occur. It is difficult for many nanoparticles to disperse uniformly in the steel. In the case of a large deformation, the second phase of agglomeration often becomes the source of cracks. This is why the strength and plasticity of the steel with 0.018 wt.% $\text{TiC}_x\text{-TiB}_2$ nanoparticles are simultaneously improved, while the strength of the steel with 0.054 wt.% $\text{TiC}_x\text{-TiB}_2$ nanoparticles is greatly increased but the fracture strain drops. The smaller grain size means more grain boundary area and more zigzag grain boundary, which is not conducive to the crack propagation. Therefore, the impact performance of the steel with 0.018 wt.% $\text{TiC}_x\text{-TiB}_2$ nanoparticles is improved. For the steels with 0.054 wt.% $\text{TiC}_x\text{-TiB}_2$ nanoparticles, the enhancement caused by grain refinement does not offset the damage of the poorly dispersed particles to impact toughness.

4. Conclusions

Trace biphasic $\text{TiC}_x\text{-TiB}_2$ nanoparticle-reinforced steels are innovatively produced by adding nanosized $\text{TiC}_x\text{-TiB}_2/\text{Al}$ master alloy during the casting process. The pearlitic-ferrite structure of the as-cast steels and the bainite structure of the steels after heat treatment have been refined and the dispersed nanosized carbides are increased. The average grain size is refined from 9.12 μm for the 40Cr steel to 3.59 μm for the steel with 0.018 wt.% $\text{TiC}_x\text{-TiB}_2$ nanoparticles. Microstructural refinement benefits from the promotion of nucleation and inhibition of dendrite growth by $\text{TiC}_x\text{-TiB}_2$ nanoparticles. Compared with the 40Cr steel ($\sigma_{0.2} = 1080$ MPa, $\sigma_{\text{UTS}} = 1120$ MPa, $\epsilon_f = 9\%$, $ak = 18.2$ J/cm², HRC = 38), the yield strength (1246 MPa), tensile strength (1469 MPa), fracture strain (9.4%), impact toughness (20.3 J/cm²), and hardness of the steel containing 0.018 wt.% $\text{TiC}_x\text{-TiB}_2$ nanoparticles are increased by 15.4%, 31.2%, 4.4%, 11.5%, and 7.9%, respectively. The yield strength (1415 MPa) and tensile strength (1554 MPa) of the steel with 0.054 wt.% $\text{TiC}_x\text{-TiB}_2$ nanoparticles are increased by 31% and 38.8% compared with the 40Cr steel, respectively. The improved tensile properties may be attributed to fine grain strengthening and the pinning effect of nanosized carbides on dislocations and grain boundaries. The results indicate that the trace $\text{TiC}_x\text{-TiB}_2$ nanoparticles are successfully introduced into the cast steel through the method of adding nanosized $\text{TiC}_x\text{-TiB}_2/\text{Al}$ master alloy during the casting process and that trace (0.018 wt.%) $\text{TiC}_x\text{-TiB}_2$ nanoparticles can simultaneously improve the strength, toughness, as well as ductility of the cast steel.

Author Contributions: Conceptualization, C.-L.L., F.Q. and Q.-C.J.; Data curation, C.-L.L. and F.Q.; Formal analysis, C.-L.L., F.Q., F.C., X.-M.Z., R.G., H.-Y.Y. and Q.-L.Z.; Investigation, C.-L.L., F.Q., F.C., X.-M.Z. and R.G.; Supervision, C.-L.L. and F.Q.; Writing—review & editing, C.-L.L., F.Q. and Q.-C.J.

Funding: This research received no external funding.

Acknowledgments: This work is supported by the National Natural Science Foundation of China (NNSFC, No. 51571101 and No. 51771081), the Source Innovation Plan of Qingdao City, China (No. 18-2-2-1-jch), the Science and Technology Development Program of Jilin Province, China (20170101178JC) and the Project 985-High Properties Materials of Jilin University.

Conflicts of Interest: The authors declare no conflict of interest.

References

1. Hong, S.-M.; Park, E.-K.; Park, J.-J.; Lee, M.-K.; Gu Lee, J. Effect of nano-sized TiC particle addition on microstructure and mechanical properties of SA-106B carbon steel. *Mater. Sci. Eng. A* **2015**, *643*, 37–46. [[CrossRef](#)]
2. Xu, Z.; Liang, G.; Guan, Q.; Jiang, Q. TiC as heterogeneous nuclei of the (Fe, Mn)₃C and austenite intergrowth eutectic in austenite steel matrix wear resistant composite. *Mater. Res. Bull.* **2004**, *39*, 457–463. [[CrossRef](#)]
3. Akhtar, F. Microstructure evolution and wear properties of in situ synthesized TiB₂ and TiC reinforced steel matrix composites. *J. Alloys Compd.* **2008**, *459*, 491–497. [[CrossRef](#)]
4. Fedrizzi, A.; Pellizzari, M.; Zadra, M.; Marin, E. Microstructural study and densification analysis of hot work tool steel matrix composites reinforced with TiB₂ particles. *Mater. Charact.* **2013**, *86*, 69–79. [[CrossRef](#)]
5. Wang, K.; Jiang, H.Y.; Wang, Y.X.; Wang, Q.D.; Ye, B.; Ding, W.J. Microstructure and mechanical properties of hypoeutectic Al–Si composite reinforced with TiCN nanoparticles. *Mater. Des.* **2016**, *95*, 545–554. [[CrossRef](#)]
6. Zhu, H.-W.; Xu, K.; Qin, S.; Xiao, F.-R.; Liao, B. Effect of heat treatment on microstructure and properties of 1045 steel modified with (NbTi)C nanoparticles. *Mater. Sci. Eng. A* **2018**, *728*, 175–182. [[CrossRef](#)]
7. Qiu, F.; Gao, X.; Tang, J.; Gao, Y.-Y.; Shu, S.-L.; Han, X.; Li, Q.; Jiang, Q.-C. Microstructures and tensile properties of Al–Cu matrix composites reinforced with nano-sized sicp fabricated by semisolid stirring process. *Metals* **2017**, *7*, 49. [[CrossRef](#)]
8. Mei, Z.; Yan, Y.W.; Cui, K. Effect of matrix composition on the microstructure of in situ synthesized TiC particulate reinforced iron-based composites. *Mater. Lett.* **2003**, *57*, 3175–3181. [[CrossRef](#)]
9. Akhtar, F.; Guo, S.J. Microstructure, mechanical and fretting wear properties of TiC-stainless steel composites. *Mater. Charact.* **2008**, *59*, 84–90. [[CrossRef](#)]
10. Lazarova, R.; Petrov, R.H.; Gaydarova, V.; Davidkov, A.; Alexeev, A.; Manchev, M.; Manolov, V. Microstructure and mechanical properties of P265GH cast steel after modification with TiCN particles. *Mater. Des.* **2011**, *32*, 2734–2741. [[CrossRef](#)]
11. Cha, L.; Lartigue-Korinek, S.; Walls, M.; Mazerolles, L. Interface structure and chemistry in a novel steel-based composite Fe–TiB₂ obtained by eutectic solidification. *Acta Mater.* **2012**, *60*, 6382–6389. [[CrossRef](#)]
12. Greer, A.L. Overview: Application of heterogeneous nucleation in grain-refining of metals. *J. Chem. Phys.* **2016**, *145*, 211704. [[CrossRef](#)] [[PubMed](#)]
13. AlMangour, B.; Baek, M.-S.; Grzesiak, D.; Lee, K.-A. Strengthening of stainless steel by titanium carbide addition and grain refinement during selective laser melting. *Mater. Sci. Eng. A* **2018**, *712*, 812–818. [[CrossRef](#)]
14. Tian, W.-S.; Zhao, Q.-L.; Zhang, Q.-Q.; Qiu, F.; Jiang, Q.-C. Simultaneously increasing the high-temperature tensile strength and ductility of nano-sized TiC_p reinforced Al–Cu matrix composites. *Mater. Sci. Eng. A* **2018**, *717*, 105–112. [[CrossRef](#)]
15. Tian, W.-S.; Zhao, Q.-L.; Zhang, Q.-Q.; Qiu, F.; Jiang, Q.-C. Enhanced strength and ductility at room and elevated temperatures of Al–Cu alloy matrix composites reinforced with bimodal-sized TiC_p compared with monomodal-sized TiC_p. *Mater. Sci. Eng. A* **2018**, *724*, 368–375. [[CrossRef](#)]
16. Park, J.-J.; Hong, S.-M.; Park, E.-K.; Kim, K.-Y.; Lee, M.-K.; Rhee, C.-K. Microstructure and properties of SA 106B carbon steel after treatment of the melt with nano-sized TiC particles. *Mater. Sci. Eng. A* **2014**, *613*, 217–223. [[CrossRef](#)]
17. Hu, S.W.; Zhao, Y.G.; Wang, Z.; Li, Y.G.; Jiang, Q.C. Fabrication of in situ TiC locally reinforced manganese steel matrix composite via combustion synthesis during casting. *Mater. Des.* **2013**, *44*, 340–345. [[CrossRef](#)]
18. Vallauri, D.; Atías Adrián, I.C.; Chrysanthou, A. TiC–TiB₂ composites: A review of phase relationships, processing and properties. *J. Eur. Ceram. Soc.* **2008**, *28*, 1697–1713. [[CrossRef](#)]
19. Grütznér, S.; Krüger, L.; Radajewski, M.; Schneider, I. Characterization of in-situ TiB/TiC particle-reinforced Ti-5Al-5Mo-5V-3Cr matrix composites synthesized by solid-state reaction with B₄C and graphite through SPS. *Metals* **2018**, *8*, 377. [[CrossRef](#)]

20. Kumar, R.; Chaubey, A.; Maity, T.; Prashanth, K. Mechanical and tribological properties of Al₂O₃-TiC composite fabricated by spark plasma sintering process with metallic (Ni, Nb) binders. *Metals* **2018**, *8*, 50. [[CrossRef](#)]
21. Li, B.; Liu, Y.; Li, J.; Cao, H.; He, L. Effect of sintering process on the microstructures and properties of in situ TiB₂-TiC reinforced steel matrix composites produced by spark plasma sintering. *J. Mater. Process. Technol.* **2010**, *210*, 91–95. [[CrossRef](#)]
22. Zhu, H.; Dong, K.; Wang, H.; Huang, J.; Li, J.; Xie, Z. Reaction mechanisms of the TiC/Fe composite fabricated by exothermic dispersion from Fe-Ti-C element system. *Powder Technol.* **2013**, *246*, 456–461. [[CrossRef](#)]
23. Lee, S.H.; Hong, S.M.; Han, B.S.; Park, J.J.; Lee, J.K.; Lee, J.G.; Lee, M.K.; Rhee, C.K. Homogeneous dispersion of TiC nano particles in a cast carbon steel matrix. *J. Nanosci. Nanotechnol.* **2010**, *10*, 258–262. [[CrossRef](#)] [[PubMed](#)]
24. Cojocaru, V.D.; Răducanu, D.; Angelescu, M.L.; Vintilă, A.N.; Șerban, N.; Dan, I.; Cojocaru, E.M.; Cinca, I. Influence of solution treatment duration on microstructural features of an industrial forged UNS S32750/1.4410/F53 super duplex stainless steel (SDSS). *Alloys JOM* **2017**, *69*, 1439–1445. [[CrossRef](#)]
25. Cojocaru, V.; Șerban, N.; Angelescu, M.; Cotruș, M.; Cojocaru, E.; Vintilă, A. Influence of solution treatment temperature on microstructural properties of an industrially forged UNS S32750/1.4410/F53 super duplex stainless steel (SDSS) alloy. *Metals* **2017**, *7*, 210. [[CrossRef](#)]
26. Angelescu, M.; Cojocaru, V.; Șerban, N.; Cojocaru, E. Evaluation of optimal forging temperature range for an industrial UNS S32750 SDSS alloy using SEM-EBSD analysis. *Metals* **2018**, *8*, 496. [[CrossRef](#)]
27. AlMangour, B.; Grzesiak, D.; Yang, J.-M. Nanocrystalline TiC-reinforced H13 steel matrix nanocomposites fabricated by selective laser melting. *Mater. Des.* **2016**, *96*, 150–161. [[CrossRef](#)]
28. Zhao, J.; Jiang, Z.; Lee, C.S. Enhancing impact fracture toughness and tensile properties of a microalloyed cast steel by hot forging and post-forging heat treatment processes. *Mater. Des.* **2013**, *47*, 227–233. [[CrossRef](#)]
29. Seok, M.-Y.; Choi, I.-C.; Moon, J.; Kim, S.; Ramamurty, U.; Jang, J.-I. Estimation of the Hall-Petch strengthening coefficient of steels through nanoindentation. *Scr. Mater.* **2014**, *87*, 49–52. [[CrossRef](#)]
30. Han, Y.; Shi, J.; Xu, L.; Cao, W.Q.; Dong, H. TiC precipitation induced effect on microstructure and mechanical properties in low carbon medium manganese steel. *Mater. Sci. Eng. A* **2011**, *530*, 643–651. [[CrossRef](#)]
31. Honga, S.G.; Kangb, K.B.; Parka, C.G. Strain-induced precipitation of NbC in Nb and Nb-Ti microalloyed HSLA steels. *Scr. Mater.* **2002**, *46*, 163–168. [[CrossRef](#)]
32. Arzt, E. Size effects in materials due to microstructural and dimensional constraints: A comparative review. *Acta Mater.* **1998**, *46*, 5611–5626. [[CrossRef](#)]
33. Wang, T.-P.; Kao, F.-H.; Wang, S.-H.; Yang, J.-R.; Huang, C.-Y.; Chen, H.-R. Isothermal treatment influence on nanometer-size carbide precipitation of titanium-bearing low carbon steel. *Mater. Lett.* **2011**, *65*, 396–399. [[CrossRef](#)]

